Semi-implicit finite volume scheme for image processing in 3D cylindrical geometry

Karol Mikula*, Fiorella Sgallari†

Abstract

Nowadays, 3D echocardiography is a well assessed instrument in medical diagnosis, in particular low-cost echocardiographic acquizition devices scan 2D slices rotated along prescribed direction. Then the discrete 3D image information is given on cylindrical grid. Usually, this original discrete image intensity function is interpolated to uniform rectangular grid and then numerical schemes for 3D image processing operations (e.g. nonlinear smoothing) in the uniform rectangular geometry are used. However, due to large amount of noise present in echocardiographic images, the interpolation step can yield undesirable results. In this paper, we avoid such step and suggest 3D finite volume method for image selective smoothing directly in the cylindrical image geometry. Namely, we study semi-implicit 3D cylindrical finite volume scheme for solving Perona-Malik-type nonlinear diffusion equation and apply the scheme to 3D cylindrical echocardiographic images. The L_∞-stability and convergence of the scheme to the weak solution of regularized Perona-Malik equation is proved.

Keywords: partial differential equations, nonlinear diffusion, finite volume method, semi-implicit scheme, image processing, cylindrical geometry, echocardiography

1 Introduction

Since the end of the 80s, the nonlinear diffusion equations have been used for processing of 2D and 3D images. After the pioneering work of Perona and Malik [15] who modified the linear heat equation ([19, 10]) to nonlinear diffusion preserving edge positions, there has been a great deal of interest in the application and analysis of such equations ([1]). One of the most important and highly growing applications is medical image processing.

For example, due to non-invasive character and ability to view anatomical structures 3D medical ultrasound (e.g. echocardiography) has become an important modality in diagnosis, assessment and management of a large number of diseases. Nevertheless, ultrasound imaging suffers from limitations that prevent its full potentiality. High amount of noise combined with low image resolution make fast denoising computational techniques necessary likewise due to the fact that the low-cost echocardiographic acquizition devices are now common instruments of real time clinical use ([6], [4]). Using a nonlinear

*Department of Mathematics, Slovak University of Technology, Radlinského 11, 813 68 Bratislava, Slovakia (e-mail: mikula@vox.svf.stuba.sk)

†Department of Mathematics, University of Bologna, Piazza di Porta S. Donato 5, 40127 Bologna, Italy (e-mail: sgallari@dm.unibo.it)

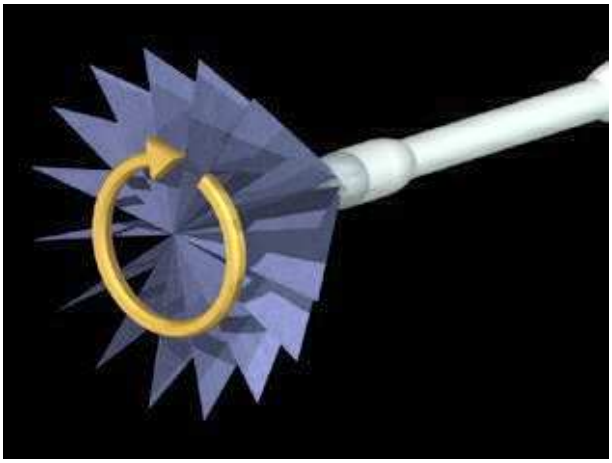

Figure 1: The echocardiographic acquizition device.

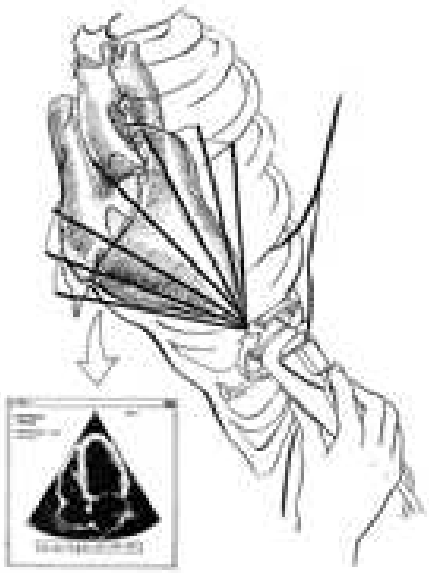

Figure 2: A schematic picture of acquizition; original rotational data information given in discrete cuttings of cone is in every rotating plane just supplemented by black color to have rotating rectangular 2D slices which give together discrete 3D cylindrical geometry.

Perona-Malik-type diffusion equations [15] is a challenging method. In our computational approach we use structure of 2D slices acquired along nonaligned rotating planes by the echocardiographic acquizition device (see Figures 1 and 2). We avoid the interpolation step on very noisy data to obtain a regular cartesian lattice ([2]) and provide image selective smoothing in the given discrete 3D cylindrical structure. Let us note that also a more general 4D (3D+time) echocardiographic image anisotropic filtering ([17]) and 3D/4D segmentation models ([13]) can be realized in cylindrical geometry using ideas of this paper, allowing computational time gain and more detailed surface rendering and 3D volume analysis/display which will be an objective of future research work.

In this paper we consider following Perona-Malik-type nonlinear PDE [3] suggested by Catté, Lions, Morel and Coll for image selective smoothing

$$u_t - \nabla.(g(|\nabla G_\sigma * u|)\nabla u) = 0. \tag{1}$$

Here, $u(t,x)$ is an unknown function defined in $Q_T \equiv [0,T] \times \Omega$, where $I = [0,T]$ is so-called scaling interval and Ω is a cylindrical domain, i.e. domain any horizontal cut of which is indicated in Figure 3. Due to natural image processing constrain to conserve a mass of the image intensity ([18]) the equation (1) is accompanied by zero Neumann boundary condition

$$\frac{\partial u}{\partial \nu} = 0 \quad \text{on} \quad I \times \partial\Omega, \tag{2}$$

where ν is the unit normal vector to the boundary of Ω. The initial condition

$$u(0,x) = u^0(x) \quad \text{in} \quad \Omega \tag{3}$$

is given by the processed image u^0. We assume that

$$g : I\!R_0^+ \to I\!R^+ \text{ is a nonincreasing function}, \quad g(\sqrt{s}) \text{ is smooth}, \tag{4}$$
$$g(0) = 1, \quad \text{and we admit } g(s) \to 0 \text{ for } s \to \infty,$$
$$G_\sigma \in C^\infty(I\!R^d) \text{ is a smoothing kernel , e.g. the Gauss function}, \tag{5}$$
$$G_\sigma(x) \to \delta_x \text{ for } \sigma \to 0, \quad \delta_x \text{ is the Dirac measure at the point } x,$$
$$u^0 \in L_\infty(\Omega), \tag{6}$$

and

$$\nabla G_\sigma * u = \int_{I\!R^d} \nabla G_\sigma(x-\xi)\tilde{u}(\xi)\, d\xi, \tag{7}$$

where $\tilde{u}$ is an extension of u by 0 from Ω to $I\!R^3$.

The equation (1) represents a modification of the original Perona-Malik model [15, 9]

$$u_t - \nabla.(g(|\nabla u|)\nabla u) = 0, \tag{8}$$

called also *anisotropic diffusion* in the computer vision community. Perona and Malik introduced equation (8) in the context of image smoothing and edge enhancement. The equation selectively diffuses the image in the regions where the signal has small variance

in intensity in contrast with those regions where the signal changes its tendency. Such a diffusion process is governed by the shape of the diffusion coefficient given by the function g in (4) and by its dependence on ∇u, which is understood as an edge indicator [15]. Since $g \to 0$ for large gradients, the diffusion is strongly slowed down on edges, while outside them it provides averaging of pixel intensities as in the linear case. From a mathematical point of view, for practical choices of g (e.g. $g(s) = 1/(1+s^2)$, $g(s) = e^{-s^2}$), the original Perona-Malik equation can behave locally like the backward heat equation. It is, in general, an ill-posed problem which suffers from non-uniqueness and whose solvability is a difficult problem [9]. One way to overcome this mathematical disadvantage has been proposed by Catté, Lions, Morel and Coll in [3]. They introduced the convolution with the Gaussian kernel G_σ into the decision process for the value of the diffusion coefficient. Since convolution with the Gaussian is equivalent to linear diffusion, their model combines ideas of linear and nonlinear scale space equations. Such a slight modification made it possible to prove the existence and uniqueness of solutions for the modified equation, and to keep the practical advantages of the original formulation. Moreover, usage of the *Gaussian gradient* $\nabla G_\sigma * u$ combines the theoretical and implementation aspects of the model. The convolution (with prescribed σ) gives a unique way to compute gradients of a piecewise constant image. It also bounds (depending on σ) the gradient of the solution as input of the function g in the continuous model—which corresponds to the situation in numerical implementations where gradients evaluated on a discrete grid are finite. Also, using the convolution, the local edge enhancement is more understandable in the presence of noise.

In Section 2 we introduce semi-implicit finite volume scheme for solving regularized Perona-Malik equation (1) in 3D cylindrical geometry and prove its convergence to the weak solution of the problem. In Section 3 we present numerical experiments computed by the scheme especially in the case of 3D echocardiography.

2 The numerical scheme

Let us have l rotating 2D slices with $m \times n$ discrete points where m is horizontal and n vertical dimension, respectively. Usually m is even, i.e. the slices do not have common intersecting discrete point. We embed this discrete structure into the finite volume mesh in such a way that every discrete point is a *representative* inner "central" *point* of 3D finite volume. A horizontal cut of such mesh is depicted in Figure 3 for $l = 4$ and $m = 10$. In the Figure, the circular points represents the acquisition nodes while dashed lines give the structure of our finite volumes around these points. In Figure 3 one can see also a dual grid given by solid lines which connect the representative points of the finite volumes.

From notational point of view, let $\mathcal{T}_h$ be such a finite volume mesh of Ω. For every pair $(p,q) \in \mathcal{T}_h^2$ with $p \neq q$, we denote their common interface by e_{pq}, i.e. $e_{pq} = \overline{p} \cap \overline{q}$ which is supposed to be included in a hypersurface of $\mathbb{R}^3$ not intersecting either p or q. In our case, a horizontal cut of e_{pq} is either straight line or arc. Let $m(e_{pq})$ denote the measure of e_{pq}, and $n_{pq}(x)$ the unit vector normal to e_{pq} at point $x \in e_{pq}$ oriented from p to q. We denote by $\mathcal{E}$ the set of pairs of adjacent control volumes, defined by $\mathcal{E} = \{(p,q) \in \mathcal{T}_h^2,\ p \neq q,\ m(e_{pq}) \neq 0\}$. We also use the notation $N(p) = \{q, (p,q) \in \mathcal{E}\ \}$. We denote by x_p, $p \in \mathcal{T}_h$, the representative point of the finite volume p, by σ_{pq} the co-edge

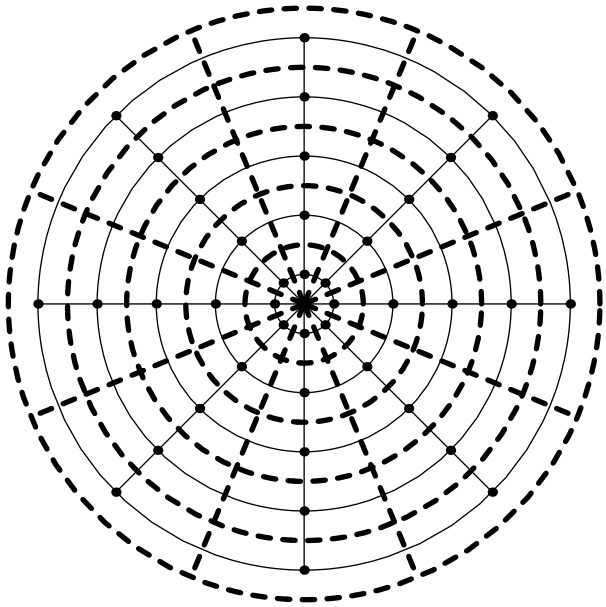

Figure 3: The horizontal cut of finite volume cylindrical grid.

of the interface e_{pq}, i.e. the part of the dual grid connecting x_p and x_q (this is again either straight line or arc) and by x_{pq} the point of intersection of e_{pq} and σ_{pq}. Let $\delta(p)$ denote the diameter of the control volume p, $m(p)$ the measure in $\mathbb{R}^3$ of the control volume p, ∂p its boundary and let $h = \max_{p \in \mathcal{T}_h} \delta(p)$.

In order to derive discrete finite volume numerical scheme in cylindrical geometry we start by the semi-discretization in scale of the problem given by (1). Choosing $N \in \mathbb{N}$ we obtain the length of the uniform discrete scale step $k = T/N$. We replace the scale derivative in (1) by backward difference. The nonlinear term of the equation is treated from the previous scale step while the linear terms are considered at the current scale level—this means semi-implicitness of the method ([8, 7, 18]). In such a way we get for every $n = 1, \ldots, N$ the equation

$$\frac{u^n - u^{n-1}}{k} - \nabla.(g(|\nabla G_\sigma * u^{n-1}|)\nabla u^n) = 0 \tag{9}$$

for an unknown function u^n, an approximation of the image intensity at the n-th discrete scale step $t_n = nk$.

Let us denote by $\overline{u}_p^n$ the representative value of u^n for the 3D finite volume p. In order to derive spatial discretization, we integrate (9) over a finite volume p

$$\int_p \frac{u^n - u^{n-1}}{k}\, dx = \int_p \nabla.\left(g(|\nabla G_\sigma * u^{n-1}|)\nabla u^n\right)\, dx. \tag{10}$$

Using the divergence theorem on the right-hand side we get

$$\int_p \nabla.\left(g(|\nabla G_\sigma * u^{n-1}|)\nabla u^n\right)\, dx = \int_{\partial p} g(|\nabla G_\sigma * u^{n-1}|)\frac{\partial u^n}{\partial \nu}\, ds =$$

$$\sum_{q\in N(p)} \int_{e_{pq}} g(|\nabla G_\sigma * u^{n-1}|) \frac{\partial u^n}{\partial \nu}\, ds.$$

Then, by means of $\overline{u}_p$ we approximate normal derivative along the boundary of p, namely $\frac{\partial u^n}{\partial \nu} \approx \frac{\overline{u}_q^n - \overline{u}_p^n}{m(\sigma_{pq})}$ along e_{pq}. The value of diffusion coefficient along e_{pq} is approximated by its value at the point x_{pq}. Since the dual grid and the boundary of finite volumes contain curvilinear parts, there is a difference between standard "polygonal" finite volume method ([5], [12]) described in mathematical literature and the method presented in this paper. However, our approach follows the lines given in the standard engineering sources (see e.g. [14] - Section 4.6.2).

Linear semi-implicit fully discrete finite volume scheme: *For $n = 1, \ldots, N$ we look for $\overline{u}_p^n$, $p =\in \mathcal{T}_h$, satisfying the equation*

$$\frac{m(p)}{k}\overline{u}_p^n + \sum_{q\in N(p)} g_{pq}^{\sigma,n-1} \frac{m(e_{pq})}{m(\sigma_{pq})}(\overline{u}_p^n - \overline{u}_q^n) = \frac{m(p)}{k}\overline{u}_p^{n-1} \tag{11}$$

starting with a given discrete image

$$\overline{u}_p^0 = \frac{1}{m(p)} \int_p u^0\,(x)\; dx, \quad p \in \mathcal{T}_h, \tag{12}$$

which is undestood as piecewise constant approximation of continuous image intensity u^0. In (11),

$$g_{pq}^{\sigma,n-1} = g(|\nabla G_\sigma * \tilde{u}_{h,k}(x_{pq}, t_{n-1})|) \tag{13}$$

where $\tilde{u}_{h,k}$ is an extension by 0 outside of Ω of the piecewise constant function $\overline{u}_{h,k}$ defined as follows

$$\overline{u}_{h,k}(x,t) = \sum_{n=0}^{N} \sum_{p\in\mathcal{T}_h} \overline{u}_p^n \chi_{\{x\in p\}} \chi_{\{t_{n-1}<t\le t_n\}} \tag{14}$$

with the boolean function $\chi_{\{A\}} = \begin{cases} 1 & \text{if } A \text{ is true} \\ 0 & \text{elsewhere.} \end{cases}$

Now, we restrict our attention to specific situation depicted in Figure 3 and write particular coefficients of the scheme in 3D cylindrical case. For that goal we define indexes $i = 1, \ldots, n_1$, $j = 1, \ldots, n_2$, $k = 1, \ldots, n_3$ in radial, angular and vertical directions of the cylindrical coordinate system. In our case $n_1 = \frac{m}{2}$, $n_2 = 2l$, $n_3 = n$ and we define $h_1 = \frac{1}{n_1}$, $h_2 = \frac{2\pi}{n_2}$, $h_3 = \frac{1}{n_3}$. The measure of the finite volume p corresponding to triple (i,j,k) is given by $m(p) = m_{ijk} = \frac{2i-1}{2} h_1^2 h_2 h_3$ and we will denote, for the moment, $\overline{u}_p^n$ corresponding value by $\overline{u}_{ijk}^n$. We can define W_{ijk}, E_{ijk}, S_{ijk}, N_{ijk}, B_{ijk}, T_{ijk} giving transmisivity coefficients $g_{pq}^{\sigma,n-1} \frac{m(e_{pq})}{m(\sigma_{pq})}$ at the sides of the finite volume $p = (i,j,k)$, $i = 1, \ldots, n_1$, $j = 1, \ldots, n_2$, $k = 1, \ldots, n_3$ by

$$W_{ijk} = g_{pq}^{\sigma,n-1}(i-1)h_2 h_3, \quad q = (i-1, j, k)$$

$$E_{ijk} = g_{pq}^{\sigma,n-1} i h_2 h_3, \quad E_{n_1 jk} = 0$$

$$S_{ijk} = g_{pq}^{\sigma,n-1} \frac{h_3}{\frac{2i-1}{2} h_2}, \quad q = (i, j-1, k)$$

$$N_{ijk} = g_{pq}^{\sigma,n-1} \frac{h_3}{\frac{2i-1}{2} h_2}, \quad q = (i, j+1, k)$$

$$B_{ijk} = g_{pq}^{\sigma,n-1} \frac{2i-1}{2} \frac{h_1^2 h_2}{h_3}, \quad q = (i, j, k-1)$$

$$T_{ijk} = g_{pq}^{\sigma,n-1} \frac{2i-1}{2} \frac{h_1^2 h_2}{h_3}, \quad q = (i, j, k+1)$$

as well as diagonal coefficients C_{ijk} and right hand sides F_{ijk}

$$C_{ijk} = \frac{m_{ijk}}{k} + W_{ijk} + E_{ijk} + S_{ijk} + N_{ijk} + B_{ijk} + T_{ijk}$$

$$F_{ijk} = \frac{m_{ijk}}{k} \overline{u}_{ijk}^{n-1}.$$

Finally, with these definitions we can write one row of the linear system (11) in the form

$$C_{ijk} \overline{u}_{ijk}^n - W_{ijk} \overline{u}_{i-1jk}^n - E_{ijk} \overline{u}_{i+1jk}^n - S_{ijk} \overline{u}_{ij-1k}^n$$

$$- N_{ijk} \overline{u}_{ij+1k}^n - B_{ijk} \overline{u}_{ijk-1}^n - T_{ijk} \overline{u}_{ijk+1}^n = F_{ijk}.$$

It is easy to see that important from image processing point of view ([18]) L_∞-stability property

$$\min_{p \in \mathcal{T}_h} \overline{u}_p^0 \le \min_{p \in \mathcal{T}_h} \overline{u}_p^n \le \max_{p \in \mathcal{T}_h} \overline{u}_p^n \le \max_{p \in \mathcal{T}_h} \overline{u}_p^0, \quad 1 \le n \le N, \tag{15}$$

can be achieved. For that goal let us write the scheme (11) in the form

$$\overline{u}_p^n + \frac{k}{m(p)} \sum_{q \in N(p)} g_{pq}^{\sigma,n-1} \frac{m(e_{pq})}{m(\sigma_{pq})} (\overline{u}_p^n - \overline{u}_q^n) = \overline{u}_p^{n-1}. \tag{16}$$

Let $\max_{r \in \mathcal{T}_h} \overline{u}_r^n$ be achieved in the node p. Then the second term on the left hand side of (16) is nonnegative and thus $\overline{u}_p^n \le \overline{u}_p^{n-1} \le \max_{r \in \mathcal{T}_h} \overline{u}_r^{n-1}$, which gives the result for max. The relation for min is derived in a similar way. The structure of (11) gives that matrix of the system is symmetric, diagonally dominant M-matrix, so there exists unique solution and preconditioned iterative linear solvers ([16]) or additive operator splitting schemes ([18]) can be used efficiently.

Remark. Using the Gauss function $G_\sigma = G_\sigma(x) = \frac{1}{(2\sqrt{\pi\sigma})^N} e^{-\frac{|x|^2}{4\sigma}}$ as the smoothing kernel, one can replace the term $G_\sigma * u^{n-1}$ by solving the linear heat equation for time σ with the initial condition given by u^{n-1}. This linear equation can be solved numerically at the same 3D cylindrical grid by one implicit step with length σ (the only difference is that $g_{pq}^{\sigma,n-1} \equiv 1$ in all above coefficients). Using that result we evaluate approximately $g_{pq}^{\sigma,n-1}$ in points x_{pq} and use these values in (11).

2.1 Definition A *weak solution* of the regularized Perona-Malik problem (1)–(3) is a function $u \in L_2(I,V)$, $V = H^1(\Omega)$ the Sobolev space, satisfying the identity

$$\int_0^T \int_\Omega u \frac{\partial \varphi}{\partial t}(x,t)\,dx\,dt + \int_\Omega u_0(x)\varphi(x,0)\,dx - \int_0^T \int_\Omega g(|\nabla G_\sigma * u|)\nabla u \nabla \varphi\,dx\,dt = 0 \quad (17)$$

for all $\varphi \in \Psi$, where Ψ is the space of smooth test functions

$$\Psi = \{\varphi \in C^{2,1}(\overline{\Omega} \times [0,T]), \nabla\varphi.\overrightarrow{n} = 0 \text{ on } \partial\Omega \times (0,T), \varphi(\cdot,T) = 0\}. \quad (18)$$

2.2 Theorem *The sequence $\overline{u}_{h,k}$ given by the sheme (11) converges strongly in $L_2(Q_T)$ to the unique weak solution u of (1)–(3) as $h,k \to 0$.*

Proof We will follow the lines of the convergence proof in [12] and outline only differences which are sufficient to solve in cylindrical case. The structure of the scheme (11) is the same as in [12] so we get a-priori estimates of the discrete solutions, which are fundamental for the convergence proof, i.e., that there exists a positive constant C, independent of h and k, such that

(i) $\max\limits_{0\le n\le N} \sum\limits_{p\in\mathcal{T}_h} (\overline{u}_p^n)^2 m(p) \le C,$

(ii) $\sum\limits_{n=1}^{N} k \sum\limits_{(p,q)\in\mathcal{E}} \frac{m(e_{pq})}{m(\sigma_{pq})}(\overline{u}_p^n - \overline{u}_q^n)^2 \le C.$

In comparison with [12] we do not work with polygonal but curvilinear finite volumes. We must take this fact into account. Let $\xi \in I\!R^d$ be a given vector. For all $(p,q) \in \mathcal{E}$, let us denote $\xi_{pq}(x) = \xi/|\xi|.n_{pq}(x)$. For all $x \in \Omega_\xi = \{x \in \Omega, [x, x+\xi] \in \Omega\}$, we denote by $E(x,p,q)$ the function defined as follows:

$$E(x,p,q) = \begin{cases} 1 & \text{if the segment } [x,x+\xi] \text{ intersects in a point } y_{pq} \text{ interface } e_{pq},\ p \\ & \text{and } q, \text{ and } \xi_{pq}(y_{pq}) > 0, \\ 0 & \text{otherwise.} \end{cases}$$

For any $t \in (0,T)$ there exists $n \in I\!N$ such that $(n-1)k < t \le nk$. Then for almost all $x \in \Omega_\xi$ we can see that

$$\overline{u}_{h,k}(x+\xi,t) - \overline{u}_{h,k}(x,t) = \overline{u}^n_{p(x+\xi)} - \overline{u}^n_{p(x)} = \sum_{(p,q)\in\mathcal{E}} E(x,p,q)(\overline{u}_q^n - \overline{u}_p^n),$$

where $p(x) \in \mathcal{T}_h$ and $x \in p$. By the Cauchy-Schwarz inequality we obtain

$$(\overline{u}_{h,k}(x+\xi,t) - \overline{u}_{h,k}(x,t))^2 \le$$
$$\le \left(\sum_{(p,q)\in\mathcal{E}} E(x,p,q)\xi_{pq}(x_{pq})m(\sigma_{pq})\right)\left(\sum_{(p,q)\in\mathcal{E}} E(x,p,q)\frac{(\overline{u}_q^n - \overline{u}_p^n)^2}{\xi_{pq}(x_{pq})m(\sigma_{pq})}\right). \quad (19)$$

Using geometrical arguments we get that $\xi_{pq}(x_{pq})m(\sigma_{pq}) = \xi/|\xi|.n_{pq}(x_{pq})m(\sigma_{pq}) = c\xi/|\xi|.(x_q - x_p)$, where $c = 1$ if σ_{pq} is straight line and $c = \frac{\pi}{n_2}/\sin(\frac{\pi}{n_2})$ if σ_{pq} is an arc. Since we have

always at least two intersecting slices in the grid, $n_2 \geq 4$ and $c \leq \frac{\pi}{2\sqrt{2}} = C$. Then again by the Cauchy-Schwarz inequality

$$\sum_{(p,q)\in\mathcal{E}} E(x,p,q)\xi_{pq}(x_{pq})m(\sigma_{pq}) \leq C\frac{\xi}{|\xi|}.(x_{p(x+\xi)} - x_{p(x)}) \leq C|x_{p(x+\xi)} - x_{p(x)}| \leq C(2h+|\xi|).$$

Now, we integrate the relation (19) on $\Omega_\xi \times (0,T)$

$$\begin{aligned}\int_{\Omega_\xi\times(0,T)} &(\overline{u}_{h,k}(x+\xi,t) - \overline{u}_{h,k}(x,t))^2\,dx\,dt \\ &\leq C(2h+|\xi|)\sum_{n=1}^{N} k \sum_{(p,q)\in\mathcal{E}} \frac{(\overline{u}_q^n - \overline{u}_p^n)^2}{\xi_{pq}(x_{pq})m(\sigma_{pq})}\int_{\Omega_\xi} E(x,p,q)\,dx\end{aligned} \tag{20}$$

and again by the geometrical argument

$$\int_{\Omega_\xi} E(x,p,q)\,dx \leq m(e_{pq})\xi.n_{pq}(x_{pq}) = m(e_{pq})\frac{\xi}{|\xi|}.n_{pq}(x_{pq})|\xi| = m(e_{pq})|\xi|\xi_{pq}(x_{pq})$$

we obtain

$$\int_{\Omega_\xi\times(0,T)} (\overline{u}_{h,k}(x+\xi,t) - \overline{u}_{h,k}(x,t))^2\,dx\,dt \leq C(2h+|\xi|)|\xi|\sum_{n=1}^{N} k \sum_{(p,q)\in\mathcal{E}} \frac{m(e_{pq})}{m(\sigma_{pq})}(\overline{u}_q^n - \overline{u}_p^n)^2. \tag{21}$$

Finally, using *a priori* estimate (ii) we get that for any vector $\xi \in I\!R^d$ there exists a positive constant C such that

$$\int_{\Omega_\xi\times(0,T)} (\overline{u}_{h,k}(x+\xi,t) - \overline{u}_{h,k}(x,t))^2\,dx\,dt \leq C|\xi|(|\xi|+2h). \tag{22}$$

Inequality (22) is called the *space translate estimate* in the finite volume methods. In the same way as in [12] we get the *time translate estimate*, i.e. that there exists a positive constant C such that for all $s \in (0,T)$

$$\int_{\Omega\times(0,T-s)} (\overline{u}_{h,k}(x,t+s) - \overline{u}_{h,k}(x,t))^2\,dx\,dt \leq Cs. \tag{23}$$

Using extension by 0 of $\overline{u}_{h,k}$ outside Ω and *discrete trace inequality* (see [5] and [12]), we can extend (22) in the following way

$$\int_{\Omega\times(0,T)} (\overline{u}_{h,k}(x+\xi,t) - \overline{u}_{h,k}(x,t))^2\,dx\,dt \leq C|\xi|. \tag{24}$$

The estimates (24) and (23) are sufficient to use following well-known *Kolmogorov's relative compactness criterion in* $L_2(Q_T)$ (see e.g. [11]):
The set $K \subset L_2(Q_T)$ is relatively compact if and only if

(i) K is bounded, i.e., there exists $C > 0$ such that $\|f\| \leq C$ for every $f \in K$;

(ii) K is mean equicontinous, i.e., for every $\varepsilon > 0$ there exists $\delta > 0$ such that

$$\int_{Q_T} (f(x+\gamma) - f(x))^2 \, dx < \varepsilon^2$$

for each $f \in K$ and γ with $|\gamma| < \delta$.

Since

$$\int_{Q_T} (\overline{u}_{h,k}(x+\xi, t+s) - \overline{u}_{h,k}(x,t))^2 \, dx \, dt$$
$$\leq 2 \int_{Q_T} (\overline{u}_{h,k}(x+\xi, t+s) - \overline{u}_{h,k}(x, t+s))^2 \, dx \, dt + 2 \int_{Q_T} (\overline{u}_{h,k}(x, t+s) - \overline{u}_{h,k}(x,t))^2 \, dx \, dt$$

using a-priori estimate (i) and estimates (24) and (23), by the Kolmogorov compactness criterion we have that there exists function $u \in L_2(Q_T)$ such that for some subsequence of $\overline{u}_{h,k}$

$$\overline{u}_{h,k} \to u \quad \text{in} \quad L_2(Q_T) \text{ as } h, k \to 0.$$

Moreover, using (22) we obtain that this limit function is in $L_2(I, V)$ ([5]) and thus it is a good candidate to be a weak solution of (1)–(3). For that goal, let $\varphi \in C_0^\infty(Q_T)$, $\varepsilon > 0$ and $\varphi(x,t) = 0$ if $|x - \partial\Omega| < \varepsilon$. Let $0 < |\xi| < \varepsilon$. Then by the Cauchy-Schwarz inequality

$$\int_{\Omega \times (0,T)} \frac{\overline{u}_{h,k}(x+\xi, t) - \overline{u}_{h,k}(x,t)}{|\xi|} \varphi(x,t) \, dx \, dt \leq \frac{\sqrt{C|\xi|(|\xi| + h)}}{|\xi|} \|\varphi\|_{L_2(Q_T)}.$$

For the limit function u we have

$$\int_{\Omega \times (0,T)} \frac{u(x+\xi, t) - u(x,t)}{|\xi|} \varphi(x,t) \, dx \, dt \leq \sqrt{C} \|\varphi\|_{L_2(Q_T)}.$$

On the other hand, by a changing of the variables $y = x + \xi$ we get

$$\begin{aligned} &\int_{\Omega \times (0,T)} \frac{u(x+\xi, t) - u(x,t)}{|\xi|} \varphi(x,t) \, dx \, dt \\ &\quad = \int_{\Omega \times (0,T)} \frac{u(y,t)}{|\xi|} \varphi(y - \xi, t) \, dy \, dt - \int_{\Omega \times (0,T)} \frac{u(y,t)}{|\xi|} \varphi(y,t) \, dy \, dt \\ &\quad = -\int_{\Omega \times (0,T)} \frac{\varphi(y,t) - \varphi(y-\xi,t)}{|\xi|} u(y,t) \, dy \, dt \\ &\quad \leq C \|\varphi\|_{L_2(Q_T)}. \end{aligned} \tag{25}$$

Let $\xi = \omega e_i$, where e_i is i-th coordinate vector, and let $\omega \to 0$. Then

$$-\int_{\Omega \times (0,T)} \frac{\partial \varphi(x,t)}{\partial x_i} u(x,t) \, dx \, dt \leq C \|\varphi\|_{L_2(Q_T)}, \quad \forall \varphi \in C_0^\infty(\Omega).$$

Thus u has generalized spatial derivatives in $L_2(Q_T)$, so it is in $L_2(I, V)$.

The last step is to prove that u fulfills the weak identity (17) from Definition 2.1, and thus it is a weak solution of the regularized Perona-Malik problem. Since such a solution

is unique due to [3], not only a subsequence of $\overline{u}_{h,k}$ but the whole sequence will converge to u. To get convergence we follow the lines of [12]-Section 3.3, with particular attention to only one step different in cylindrical case. In the proof of Lemma 3.8 of [12] we should get an estimate

$$J = \left| \frac{\varphi(x_q, t_n) - \varphi(x_p, t_n)}{m(\sigma_{pq})} - \nabla\varphi(x_{pq}, t_n).n_{pq}(x_{pq}) \right| \leq Ch \tag{26}$$

for any smooth function $\varphi \in \Psi$. It is clearly true if σ_{pq} is a straight line, so we only consider case if σ_{pq} is an arc. Then

$$\int_{\sigma_{pq}} \frac{\partial\varphi}{\partial T} ds = \varphi(x_q) - \varphi(x_p)$$

where T is the unit tangent vector to the curve σ_{pq}. By the mean value theorem there exists a point $\eta \in \sigma_{pq}$ such that

$$\nabla\varphi(\eta).T(\eta) = \frac{\varphi(x_q, t_n) - \varphi(x_p, t_n)}{m(\sigma_{pq})}.$$

Since $T(x_{pq}) = n_{pq}(x_{pq})$ we have

$$\begin{aligned} J = & \left| \tfrac{\varphi(x_q,t_n)-\varphi(x_p,t_n)}{m(\sigma_{pq})} - \nabla\varphi(\eta).T(\eta) + \nabla\varphi(\eta).T(\eta) - \nabla\varphi(x_{pq}).T(x_{pq}) \right| = \\ & |\nabla\varphi(\eta).(T(\eta) - T(x_{pq})) + (\nabla\varphi(\eta) - \nabla\varphi(x_{pq})).T(x_{pq})| \leq \\ & |\nabla\varphi(\eta)|\,|T(\eta) - T(x_{pq})| + |\nabla\varphi(\eta) - \nabla\varphi(x_{pq})|\,|T(x_{pq})| \leq Ch \end{aligned}$$

due to smoothness of φ and the fact that $|T(\eta) - T(x_{pq})| \leq \frac{\pi}{n_2} \leq Ch$ for any $\eta \in \sigma_{pq}$. □

3 Discussion on numerical experiments

In the first experiment we have computed artificial example where the simple double valued radially symmetric intensity function is perturbed by high additive noise. Such initial noisy function and the result after application of 100 scale steps of the scheme (11) is given in Figure 4. The reconstructed image perfectly corresponds to original data. We use the function

$$g(s) = \frac{1}{1 + Ks^2} \tag{27}$$

with some positive constant K; in the previous experiment $K = 2$.

Next we applied the method to real 3D cylindrical echocardiographic images given by 60 rotating slices with 240×200 pixels. It means that we have $n_1 = 120$, $n_2 = 120$, $n_3 = 200$. One can imagine from Figure 5 where we present horizontal 2D cut of data in the center of cylinder (front view (left) and top view (right)) how noisy are the original data. In Figure 6 we present results after 2 and 10 steps of the algorithm with $K = 1$. In order to not conserve undesirable edges (speckle noise) a smaller $K = 0.1$ is used for the diffusivity in the angular direction. Such results are presented in Figure 7 after the same number of scale steps.

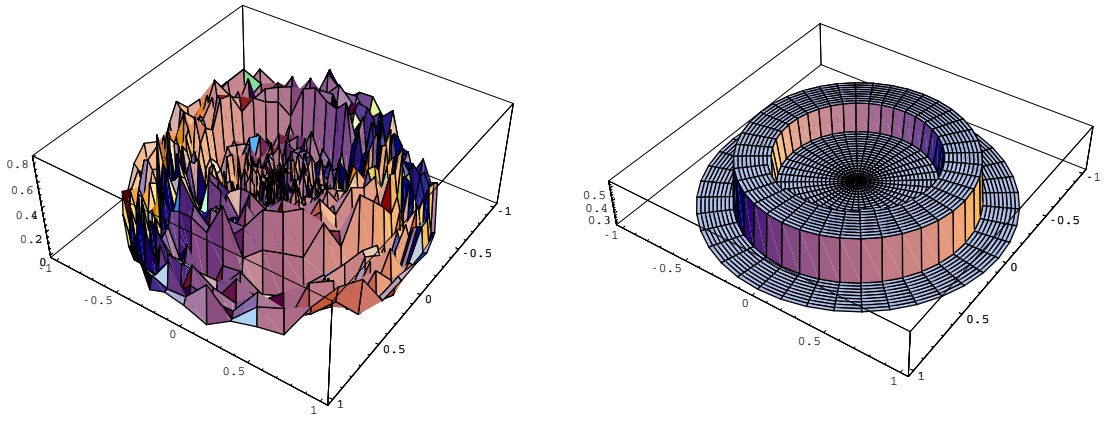

Figure 4: Horizontal cut of artificially given noisy initial data (left) and its perfect reconstruction (right).

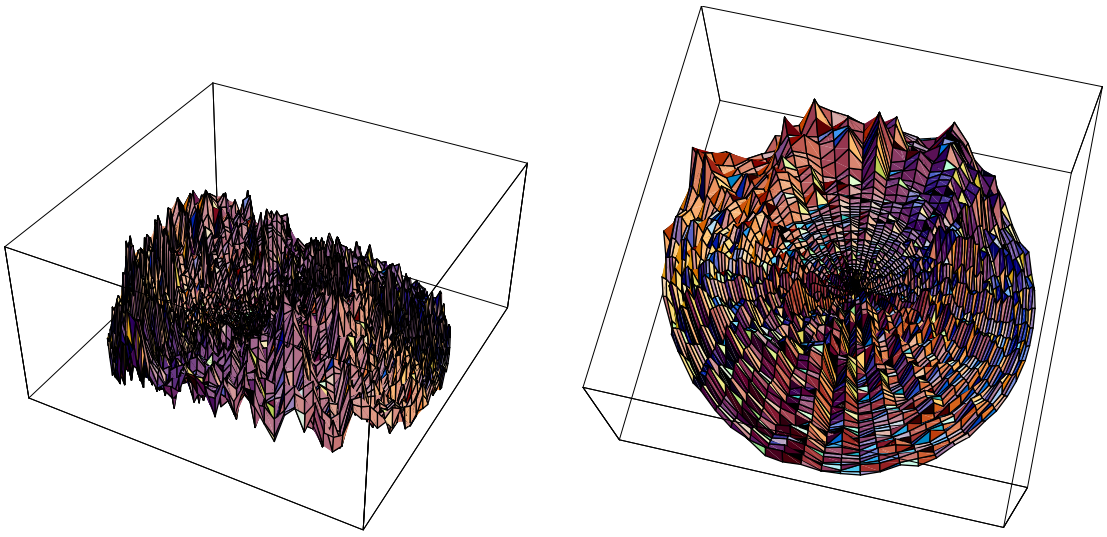

Figure 5: Horizontal cut of 3D cylindrical echocardiographic data, front view (left), top view (right).

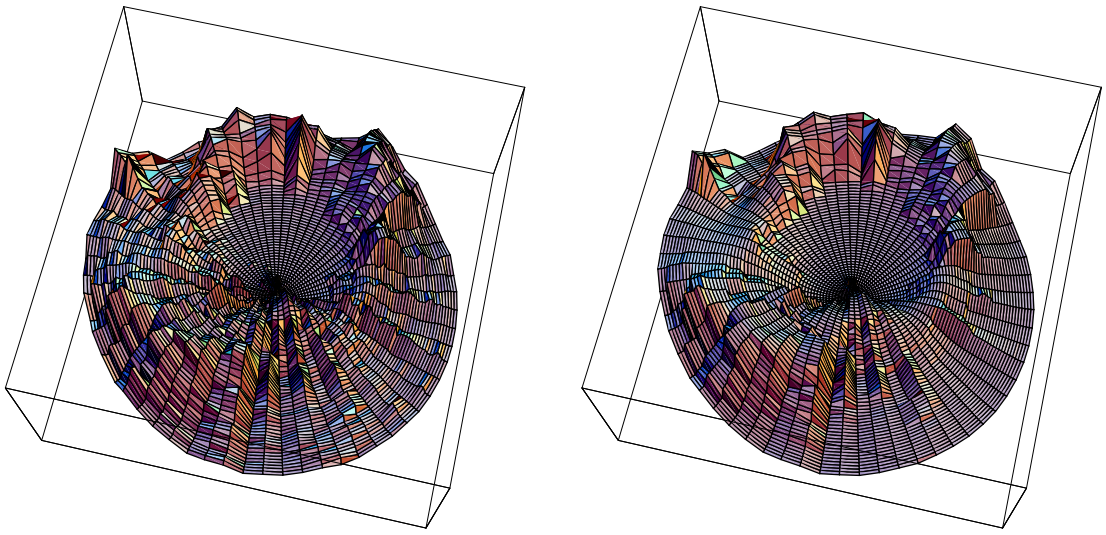

Figure 6: Smoothing of the data after 2 (left) and 10 (right) scale steps of the algorithm.

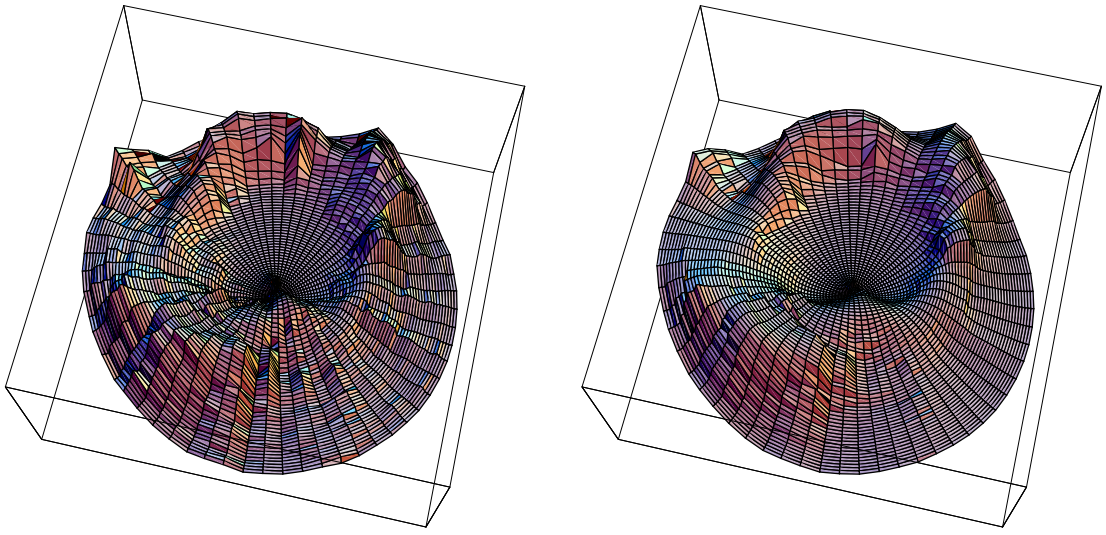

Figure 7: Smoothing of the data after 2 (left) and 10 (right) scale steps of the algorithm with stronger diffusion in angular direction.

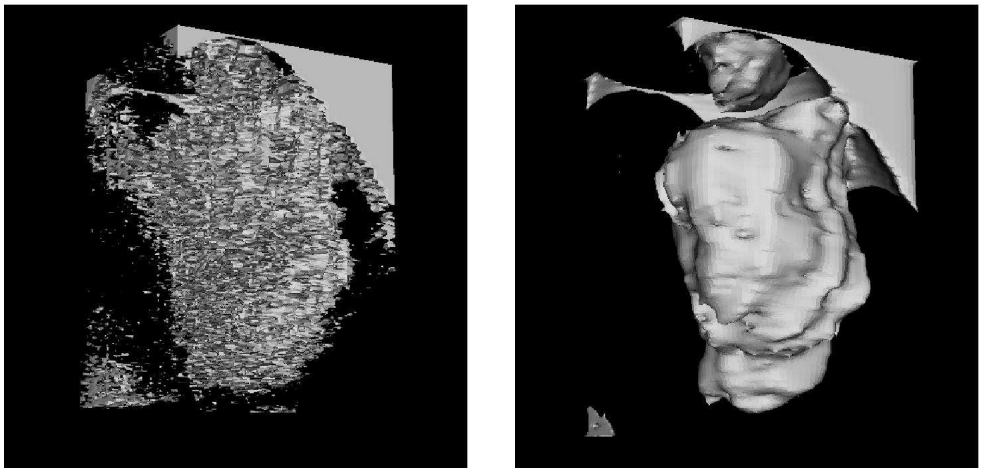

Figure 8: Ventricular boundary visualized before (left) and after (right) nonlinear image smoothing.

In Figure 8 we show visualization of the ventricular volume using original noisy data (left) and data after nonlinear smoothing by our algorithm (right). One can clearly see necessity of nonlinear filtering to get understanding of 3D ventricular shape.

Acknowledgement. We thank to ESAOTE Biomedica, Firenze, Italy, for bringing the problem to our attention and providing 3D cylindrical echocardiographic images.

References

[1] L. Alvarez, F. Guichard, P. L. Lions, and J.-M. Morel, Axioms and fundamental equations of image processing, *Arch. Rational Mech. Anal.* **123** (1993), 200–257.

[2] H.N. Cardinal, J.D. Gill, A. Fenster, Analysis of geometrical distortion and statistical variance in length, area and volume in a linearly scanned 3D ultrasound image, *IEEE Transactions on Medical Imaging*, Vol. 19, No. 6 (2000) pp 632-651

[3] F. Catté, P.L. Lions, J.-M. Morel, and T. Coll, Image selective smoothing and edge detection by nonlinear diffusion, *SIAM J. Numer. Anal.* **29** (1992), 182–193.

[4] ESAOTE Biomedica, Firenze - private communications

[5] R. Eymard, T. Gallouet, and R. Herbin, The finite volume method, Handbook of Numerical Analysis, Vol. 7 (Ph. Ciarlet, J. L. Lions, eds.), Elsevier, 2000.

[6] A. Fenster, D.B. Downey, 3-D ultrasound imaging: a review, *IEEE Engineering in Medicine and Biology Magazine*, Vol.15 Issue 6, (1996) pp. 41 -51

[7] A. Handlovičová, K. Mikula, and F. Sgallari, Variational numerical methods for solving nonlinear diffusion equations arising in image processing, *J. Visual Communication and Image Representation*, Vol. 13 (2002) pp 217-237

[8] J. Kačur and K. Mikula, Solution of nonlinear diffusion appearing in image smoothing and edge detection, *Appl. Numer. Math.* **17** (1995), 47–59.

[9] S. Kichenassamy, The Perona-Malik paradox, *SIAM J. Appl. Math.* **57** (5) (1997), 1328–1342.

[10] J. J. Koenderink, The structure of images, *Biol. Cybern.* **50** (1984), 363–370.

[11] A. Kufner, O. John, and S. Fučík, Function Spaces, Academia, Prague, 1977.

[12] K. Mikula and N. Ramarosy, Semi-implicit finite volume scheme for solving nonlinear diffusion equations in image processing, *Numer. Math.* **89** (3) (2001), 561–590.

[13] J. Montagnat, M. Sermesant, H. Delingette, G. Malandain, N. Ayache, Anisotropic filtering for model-based segmentation of 4D cylindrical echocardiographic images, *Pattern Recognition Letters* 24 (2003) pp. 815-828

[14] S.V. Patankar, Numerical heat transfer and fluid flow, Hemisphere Publ. Corp., Washington, 1980

[15] P. Perona and J. Malik, Scale space and edge detection using anisotropic diffusion, *Proc. IEEE Computer Society Workshop on Computer Vision* (1987).

[16] Y. Saad, *Iterative Methods For Sparse Linear Systems*, PWS Publ. Comp., 1996.

[17] A. Sarti, K. Mikula, F. Sgallari, Nonlinear multiscale analysis of three-dimensional echocardiographic sequences, *IEEE Transactions on Medical Imaging*, Vol. 18 (1999) pp. 453–466.

[18] J. Weickert, Anisotropic Diffusion in Computer Vision, Teubner-Stuttgart, 1998.

[19] A.P. Witkin, Scale-space filtering, *Proc. Eight Internat. Conf. on Artificial Intelligence*, Vol. 2 (1983), 1019–1022.